CANCER

Urinary detection of lung cancer in mice via noninvasive pulmonary protease profiling

Jesse D. Kirkpatrick[1,2]*, Andrew D. Warren[1,2]*, Ava P. Soleimany[1,2,3]*, Peter M. K. Westcott[1], Justin C. Voog[1,2,4], Carmen Martin-Alonso[1,2], Heather E. Fleming[1,2], Tuomas Tammela[5], Tyler Jacks[1,6], Sangeeta N. Bhatia[1,2,6,7,8,9,10]†

Lung cancer is the leading cause of cancer-related death, and patients most commonly present with incurable advanced-stage disease. U.S. national guidelines recommend screening for high-risk patients with low-dose computed tomography, but this approach has limitations including high false-positive rates. Activity-based nanosensors can detect dysregulated proteases in vivo and release a reporter to provide a urinary readout of disease activity. Here, we demonstrate the translational potential of activity-based nanosensors for lung cancer by coupling nanosensor multiplexing with intrapulmonary delivery and machine learning to detect localized disease in two immunocompetent genetically engineered mouse models. The design of our multiplexed panel of sensors was informed by comparative transcriptomic analysis of human and mouse lung adenocarcinoma datasets and in vitro cleavage assays with recombinant candidate proteases. Intrapulmonary administration of the nanosensors to a *Kras*- and *Trp53*-mutant lung adenocarcinoma mouse model confirmed the role of metalloproteases in lung cancer and enabled accurate detection of localized disease, with 100% specificity and 81% sensitivity. Furthermore, this approach generalized to an alternative autochthonous model of lung adenocarcinoma, where it detected cancer with 100% specificity and 95% sensitivity and was not confounded by lipopolysaccharide-driven lung inflammation. These results encourage the clinical development of activity-based nanosensors for the detection of lung cancer.

INTRODUCTION

Lung cancer is the most common cause of cancer-related death (25.3% of cancer deaths in the United States), with dismal 18.6% 5-year survival rates (*1*). Underlying this high mortality is the fact that 57% of patients with lung cancer have distant spread of disease at the time of diagnosis (*1*). Because patients with regional or localized disease have 6- to 13-fold higher 5-year survival rates than patients with distant metastases (*1*), substantial effort has been dedicated to early detection of lung cancer. In the United States, screening with low-dose computed tomography (LDCT) is recommended in high-risk patients [adults aged 55 to 80 years with a 30 pack-year smoking history (*2*)] and enabled a relative reduction in mortality of 20% when compared to chest radiography in the National Lung Screening Trial (NLST) (*3*). However, in addition to expense (*4*) and risks associated with radiation exposure (*5*), LDCT suffers from high false-positive rates (*3*), leading to a considerable burden of complications incurred during unnecessary follow-up procedures. Transthoracic needle biopsy, for example, is associated with a 15% rate of pneumothorax and a 6.6% rate of pneumothorax requiring chest drainage (*6*). Overall, the risk of dying or suffering a major complication in an LDCT-screened patient with a benign nodule is 4.1 and 4.5 per 10,000, respectively (*5*). As a result of these limitations, screening by LDCT has not been widely adopted outside of the United States (*7*), and there is an urgent need to develop diagnostic tests that increase the effectiveness of lung cancer screening.

Great strides in molecular diagnostics have yielded promising approaches that may be used in conjunction with or as an alternative to LDCT for lung cancer screening. Circulating tumor DNA (ctDNA) has emerged as a promising tool for noninvasive molecular profiling of lung cancer (*8*, *9*). However, the presence of ctDNA scales with tumor burden, and there are thus fundamental sensitivity limits for early-stage disease (*8*, *10*). In patients with a suspicious nodule identified by LDCT, transcriptional profiling of bronchial brushings can enhance the diagnostic sensitivity of bronchoscopy alone (*11*), leveraging the "field of injury" that results from smoking and other environmental exposures. However, as with any invasive procedure, bronchoscopy carries the risk of attendant complications such as pneumothorax (*3*, *5*).

Rather than relying on imaging or the detection of endogenous biomarkers in circulation, we have developed a class of "activity-based nanosensors" that monitor for a disease state by detecting and amplifying the activity of aberrant proteases and that function as urinary reporters (*12*–*19*). Protease activity is dysregulated in cancer, and proteases across all catalytic classes play a direct role in tumorigenesis (*20*, *21*). Activity-based nanosensors leverage dysregulated protease activity to overcome the insensitivity of previous biomarker assays, amplifying disease-associated signals generated in the tumor microenvironment and providing a concentrated urine-based readout. We have previously explored the sensitivity of this approach using mathematical modeling (*22*) and cell transplant models (*16*). However, to drive accurate diagnosis in a heterogeneous disease, a diagnostic must also be highly specific. Here, we explored the potential to attain both sensitive and specific lung cancer detection by multiplexing 14 activity-based nanosensors in two immunocompetent,

[1]Koch Institute for Integrative Cancer Research, Massachusetts Institute of Technology, Cambridge, MA 02139, USA. [2]Harvard-MIT Division of Health Sciences and Technology, Institute for Medical Engineering and Science, Massachusetts Institute of Technology, Cambridge, MA 02139, USA. [3]Harvard Graduate Program in Biophysics, Harvard University, Boston, MA 02115, USA. [4]Department of Radiation Oncology, Memorial Sloan Kettering Cancer Center, New York, NY 10065, USA. [5]Cancer Biology and Genetics Program, Sloan Kettering Institute, Memorial Sloan Kettering Cancer Center, New York, NY 10065, USA. [6]Howard Hughes Medical Institute, Cambridge, MA 02139, USA. [7]Department of Electrical Engineering and Computer Science, Massachusetts Institute of Technology, Cambridge, MA 02139, USA. [8]Department of Medicine, Brigham and Women's Hospital, Harvard Medical School, Boston, MA 02115, USA. [9]Broad Institute of Massachusetts Institute of Technology and Harvard, Cambridge, MA 02139, USA. [10]Wyss Institute at Harvard, Boston, MA 02115, USA.
*These authors contributed equally to this work.
†Corresponding author. Email: sbhatia@mit.edu

autochthonous mouse models driven by either *Kras*/*Trp53* (KP) mutations or *Eml4-Alk* (EA) fusion. Clinically, activity-based nanosensors may have utility as an alternative to invasive follow-up procedures in patients with positive LDCT findings.

RESULTS

Aberrant protease expression is induced in a *Kras*- and *Trp53*-mutant mouse model of lung adenocarcinoma

Common driver mutations of non-small cell lung cancer in humans include those that activate *KRAS* (10 to 30%) or inactivate *TP53* (50 to 70%) (*23*). To examine the ability of activity-based nanosensors to detect lung cancer in a relevant mouse model (Fig. 1), we selected a genetically driven model of adenocarcinoma that incorporates mutations in these genes. This extensively characterized model uses intratracheal administration of a virus encoding Cre recombinase to activate mutant $Kras^{G12D}$ and delete both copies of *Trp53* in the lungs [$Kras^{LSL\text{-}G12D/+}$;$Trp53^{fl/fl}$ (KP) mice; fig. S1A], initiating tumors that closely recapitulate human disease progression from alveolar adenomatous hyperplasia (AAH) to grade IV adenocarcinoma (fig. S1B) (*24*). We analyzed a recently published RNA sequencing (RNA-seq) dataset (*25*) that profiled KP tumors (n = 22) across disease stages, as well as *Kras*-mutant, *Trp53*-WT (K) tumors (n = 3) to identify proteases that were up-regulated in tumor cells relative to normal lung cells (Fig. 2A). Because this dataset profiled tumor cells sorted by flow cytometry and therefore failed to capture proteases contributed by microenvironmental immune and stromal cells, we supplemented this analysis with a bulk gene expression microarray dataset profiling K tumors (*26*), which are transcriptionally similar to early-stage KP tumors and human lung adenomas (*25*). We used significance analysis of microarrays (*27*) to identify proteases with increased expression in K model tumors relative to normal lungs (Fig. 2B).

Proteases overexpressed in the KP mouse model are relevant to human lung adenocarcinoma

To ensure that activity-based nanosensors were tuned to address human lung adenocarcinoma (LUAD)–associated proteases, we mined The Cancer Genome Atlas (TCGA) dataset (*28*) and analyzed the expression of 168 human extracellular endoprotease genes in LUAD and normal adjacent tissue (Fig. 2C) (*29*). Of the 20 most highly up-regulated proteases, 9 were metalloproteases, 11 were serine proteases, and several overlapped with proteases overexpressed in KP tumors (Fig. 2C, bottom). We found using gene set enrichment analysis (GSEA) (*30*) that the top 20 overexpressed extracellular proteases in the KP model were significantly enriched in human LUAD (P = 0.0002) (Fig. 2D), suggesting that the proteolytic landscape of the KP model recapitulated that of human disease. We then performed receiver operating characteristic (ROC) analysis on RNA-seq data curated by the Lung Genomics Research Consortium (LGRC) (*31*) and found that proteases overexpressed in human LUAD were not increased in interstitial lung disease or chronic obstructive pulmonary disease (fig. S2A). In contrast, classification efficiency in LUAD reached above 0.9 for 8 of 10 proteases (fig. S2, B to D).

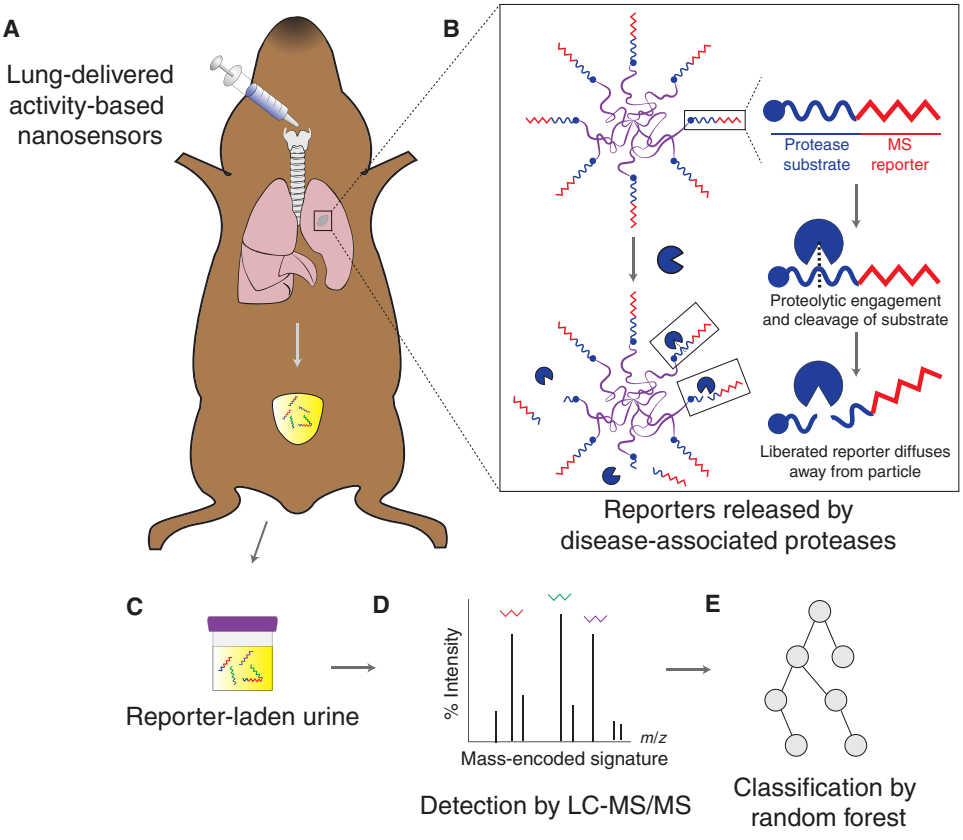

Fig. 1. Study approach and overview. (**A**) Activity-based nanosensors were administered to mice by intratracheal instillation. (**B**) At the tumor periphery, disease-associated proteases cleave protease substrates, liberating mass spectrometry (MS)–encoded reporters from the PEG scaffold. (**C** and **D**) These reporters are small enough to diffuse into the bloodstream and passively filter into the urine (C) for detection by LC-MS/MS (D). (**E**) Classification was performed on a training cohort of mice and subsequently applied to an independent test cohort to provide a positive or negative readout of malignancy.

A panel of proteases overexpressed in human and mouse LUAD enables classification of human disease

We next sought to nominate a set of proteases against which to build our nanosensor panel. We excluded any genes for which an active recombinant protease was unavailable, selected six to seven of the top 20 overexpressed genes from each dataset, removed duplicates, and arrived at a "LUAD protease panel" of 15 protease genes (Fig. 2E, and indicated in bold red text in Fig. 2, A to C). This panel included napsin A, a highly sensitive and specific immunohistochemical marker for human LUAD (*32*), and several metalloproteases known to be expressed at the protein level in human LUAD (*33*). To assess whether the expression of these 15 proteases enabled classification of LUAD from normal adjacent tissue, we built a generalized linear model (GLM) classifier using a subset of the TCGA gene expression data,

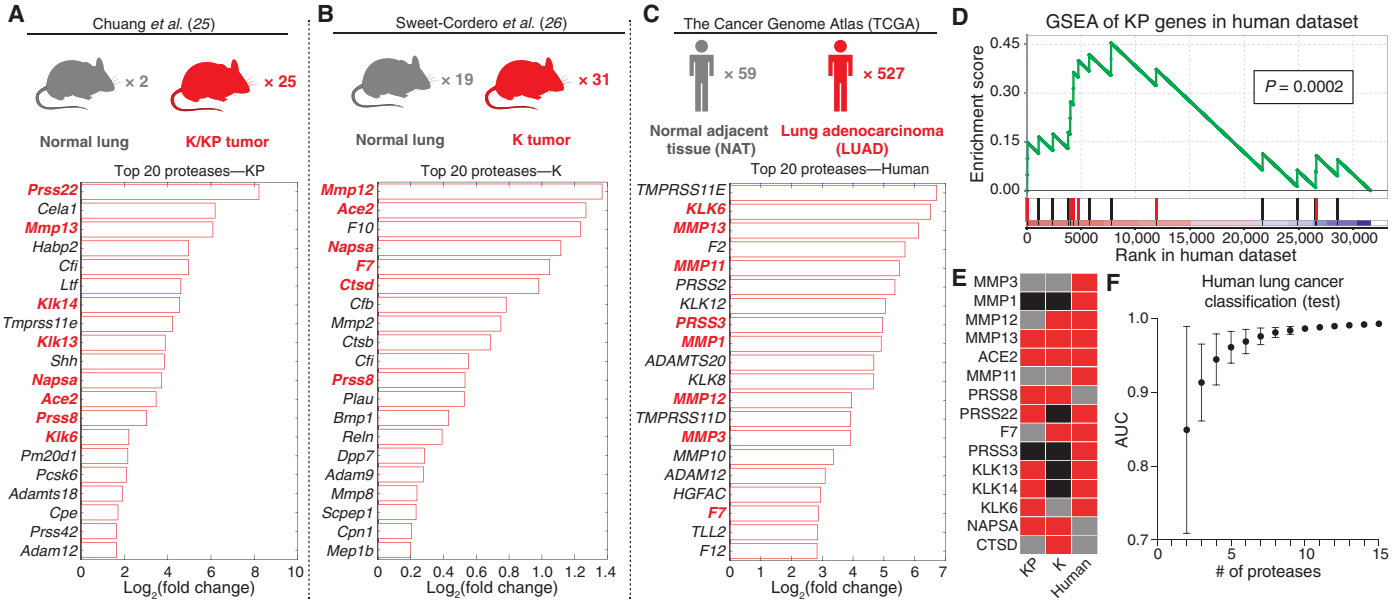

Fig. 2. Proteases are up-regulated in lung cancer and enable classification of human disease. (**A** to **C**) Existing mouse (A and B) and human (C) gene expression datasets were analyzed to identify extracellular endoproteases overexpressed in lung cancer. Protease genes in red were selected for the LUAD protease panel. (**D**) GSEA was performed in the TCGA (human) dataset using orthologs of the top 20 overexpressed protease genes in KP tumors ($P = 0.0002$). Red bars are genes included in the LUAD protease panel. (**E**) A set of 15 proteases was selected as the LUAD protease panel. Red, $Fold_{Disease} > 1$; gray, $Fold_{Disease} < 1$, where $Fold_{Disease}$ is gene expression in disease relative to control. Black, not included in the dataset. (**F**) GLM classification on the TCGA dataset using the 15 protease genes in the LUAD protease panel as features. AUC for the test cohort is shown as a function of the number of proteases included in the classifier ($n = 50$ combinations of protease genes for each point). Points are means ± SD.

applied it to an independent test cohort, and found that the area under the ROC curve (AUC) was 0.99 when all 15 proteases were used as features (Fig. 2F). In addition, as assessed by GSEA, this 15-gene panel was significantly enriched in stage I LUAD ($P < 0.0001$; fig. S3A), as well as all tested molecular subtypes of adenocarcinoma, including *KRAS*-mutant ($P < 0.0001$; fig. S3B), *TP53*-mutant ($P = 0.0002$; fig. S3C), *EGFR*-mutant ($P = 0.0004$; fig. S3D), and *BRAF*-mutant ($P = 0.0002$; fig. S3E) genetic subtypes. Last, we performed differential expression analysis of lung squamous cell carcinoma relative to normal adjacent tissue from the TCGA dataset and found significant enrichment of the same 15-protease panel by GSEA ($P = 0.0002$; fig. S3F).

Cleavage of multiplexed substrate panel follows class-specific patterns

We synthesized 14 fluorogenic peptide substrates (PPQ1 to PPQ14; table S1) that were known to encompass the cleavage preferences of metalloproteases, serine proteases, and aspartic proteases (*17*). We incubated each individual probe with each of the 15 proteases in the panel (Fig. 3A) and measured protease activity by monitoring fluorescence increase over time (Fig. 3B). Hierarchical clustering of fluorescence fold changes of each substrate revealed separation of proteases of different classes (Fig. 3C). Whereas certain probes were cleaved selectively by individual classes of proteases, such as metalloproteases for PPQ2 and serine proteases for PPQ11, other probes were cleaved by proteases of multiple classes (fig. S4). For example, in addition to being cleaved by metalloproteases, PPQ3 and PPQ12 were acted upon by aspartic proteases and serine proteases, respectively (fig. S4). Overall, the dequenching panel results indicated that the set of 14 probes provided coverage of the cleavage profiles of all three protease families represented by the LUAD protease panel.

Nanoparticles delivered into mouse airways distribute throughout the lung and reach the tumor periphery

To adapt the activity-based nanosensor platform for detection of localized lung cancer, we sought to circumvent background protease activity present in the blood and off-target organs by administering the nanosensors via localized intrapulmonary, rather than systemic intravenous, delivery. We built activity-based nanosensors using a 40-kDa eight-arm poly(ethylene glycol) (PEG-8_{40kDa}) nanoparticle coupled to protease substrates bearing terminal mass-encoded reporters (Fig. 1B). To assess biodistribution of the nanosensors following intrapulmonary delivery, we labeled the PEG-8_{40kDa} scaffold with near-infrared dye VivoTag 750 (VT750), delivered the nanoparticles to mice by intratracheal (IT) instillation or intravenous (IV) injection, and collected organs after 60 min (Fig. 4A). Fluorescence imaging revealed deep delivery of nanoparticles to all lung lobes in mice receiving intratracheal particles but negligible delivery to other organs (Fig. 4, B and C). In contrast, only 14% of organ fluorescence was confined to the lung in the intravenous-delivered group. In the intratracheally treated mice, the lung half-life of PEG-8_{40kDa} was 6.3 days (fig. S5). No toxicity was observed at either short (2 hours) or longer (24 hours and over 10 days) intervals after nanosensor administration in healthy control mice, as assessed by weight tracking (fig. S6A) and histological assessment by a veterinary pathologist (fig. S6B).

To assess microscopic distribution of the nanosensor scaffold within the lung, we labeled the PEG-8_{40kDa} scaffold with biotin and administered the nanoparticles to healthy mice by intratracheal instillation. Lungs were collected from mice 20 to 30 min after intratracheal

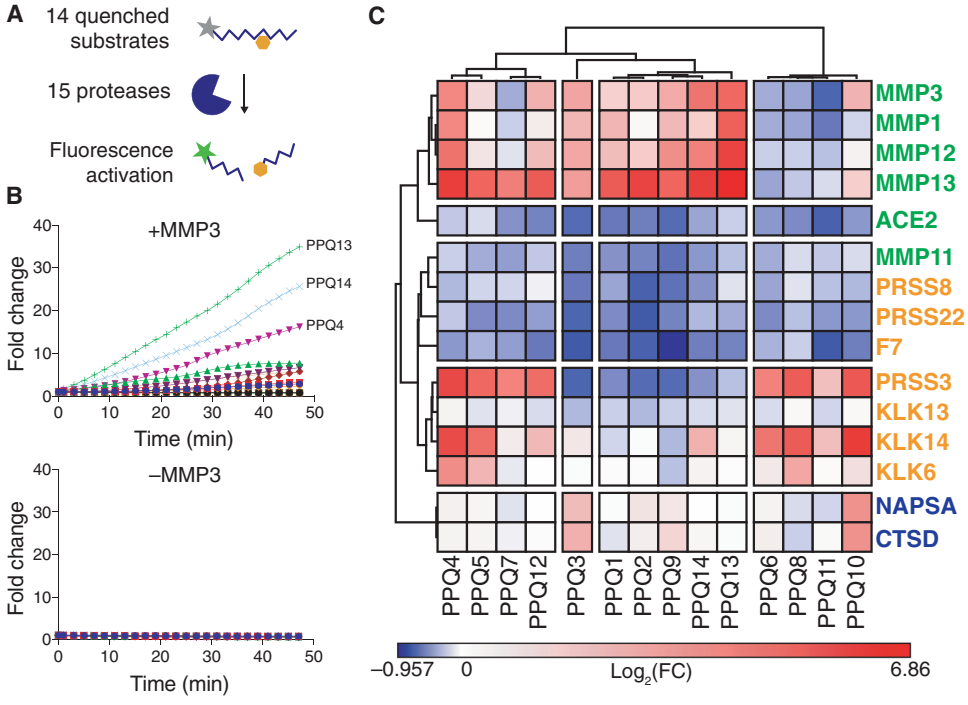

Fig. 3. LUAD substrate panel cleavage patterns are driven by protease class. (**A**) All 15 proteases in the LUAD protease panel were screened against a panel of 14 Förster resonance energy transfer (FRET)–paired protease substrates, and fluorescence activation was monitored over 45 min. (**B**) Kinetic fluorescence curves are shown for 14 FRET-paired substrates with (top) and without (bottom) addition of MMP3. (**C**) Fluorescence fold changes at 45 min (average of two replicates) were $\log_2$ transformed, and hierarchical clustering was performed to cluster proteases (vertical) by their substrate specificities and substrates (horizontal) by their protease specificities. Proteases labeled in green, orange, or blue represent metalloproteases, serine proteases, or aspartic proteases, respectively.

delivery, fixed, and stained for biotin. Whereas lungs from untreated mice were negative for biotin (Fig. 4D, top), lungs from mice that received the scaffold demonstrated broad distribution of nanoparticles throughout the lung (Fig. 4D, bottom left), specifically within terminal alveoli (Fig. 4D, bottom right).

We then administered biotin-labeled PEG-8_{40kDa} scaffold in late-stage KP tumor-bearing mice by intratracheal instillation to assess whether these particles were able to reach the site of disease. Whereas lungs from untreated KP mice were negative for biotin (Fig. 4E, top), lungs from KP mice that received intrapulmonary delivery of the biotinylated scaffold demonstrated presence of nanoparticles at the margins of tumors (Fig. 4E, bottom).

As a step toward developing a more clinically relevant delivery method, we also sought to characterize particle durability and biodistribution after aerosolization. We directly aerosolized our PEG carrier particles (fig. S7, A and B) and found no aggregation or changes in particle size distribution, as assessed by transmission electron microscopy (fig. S7, C and D) and dynamic light scattering (fig. S7E). Furthermore, PEG-PPQ5 before and after aerosolization was equally sensitive to in vitro cleavage by recombinant matrix metalloproteinase 13 (MMP13) (fig. S7F).

Last, we functionalized the PEG nanoparticles with either a near-infrared dye for biodistribution studies or biotin for histological assessment and used pressure-driven aerosolization to perform intrapulmonary administration. Gross fluorescent visualization of VT750 revealed deep penetration throughout the lung and in all lobes (fig. S8A), without distribution to other organs (fig. S8B). Histological staining of fixed lungs collected from mice 10 min after inhalation demonstrated no biotin staining in control lungs (fig. S8, C and D) but broad staining throughout the lung overall (fig. S8E) and in terminal alveoli (fig. S8F) in mice treated with aerosolized nanoparticles.

Mass-encoded reporters filter from the lung to the urine via the blood and are detectable by mass spectrometry

To enable multiplexed detection of a broad spectrum of disease-associated proteases via a single in vivo administration of nanosensors, we conjugated each member of the LUAD substrate panel to a uniquely identifiable mass-encoded reporter (PP01 to PP14; Table 1). As previously described (*12*), we used variable labeling of the 14-mer glutamate-fibrinopeptide B (Glu-Fib) with stable isotope-labeled amino acids to uniquely barcode each of the 14 peptide substrates. Multiple reaction monitoring via a liquid chromatography triple quadrupole mass spectrometer (LC-MS/MS) enabled quantitative assessment of urinary reporter concentration within a broad linear range (1 to 1000 ng/ml; fig. S9A). By administering mass-encoded free reporters by intratracheal and intravenous administration, we found that urinary accumulation scaled linearly with input doses between 2.5 and 25 ng for both routes of delivery ($\text{slope}_{IT} = 0.075\ \text{ng}^{-1}$ and $\text{slope}_{IV} = 0.077\ \text{ng}^{-1}$; fig. S9B). Administering a Cy7-labeled version of Glu-Fib, we found characteristic single-exponential concentration decay after intravenous injection and a two-phase kinetic profile after intratracheal administration (fig. S9C), suggesting an initial phase of partitioning from the alveoli into the blood (peaking at 1 to 2 hours after delivery), followed by renal filtration from the blood.

Activity-based nanosensor cleavage is dysregulated in lung cancer mouse models

We then sought to longitudinally monitor disease progression in KP mice with activity-based nanosensors and benchmark their diagnostic performance against micro-computed tomography (microCT). After initiating disease via intratracheal administration of adenovirus encoding Cre recombinase (fig. S1A), we monitored tumor development by performing microCT at 5 weeks (KP_{5wk}), 7.5 weeks ($KP_{7.5wk}$), and 10.5 weeks ($KP_{10.5wk}$) after adenoviral induction (Fig. 5A and table S2). The sensitivity of microCT at 100% specificity was 33.3% at 5 weeks, 75% at 7.5 weeks, and 100% at 10.5 weeks, and the average tumor burden at these three time points was 0.775, 2.78, and 19.2 mm^3 (Fig. 5A and table S2).

To characterize activity-based nanosensor performance in vivo relative to microCT, we administered all 14 protease-sensitive nanoparticles to the lungs of KP mice and age- and sex-matched healthy controls at 5, 7.5, and 10.5 weeks after tumor initiation. Several reporters

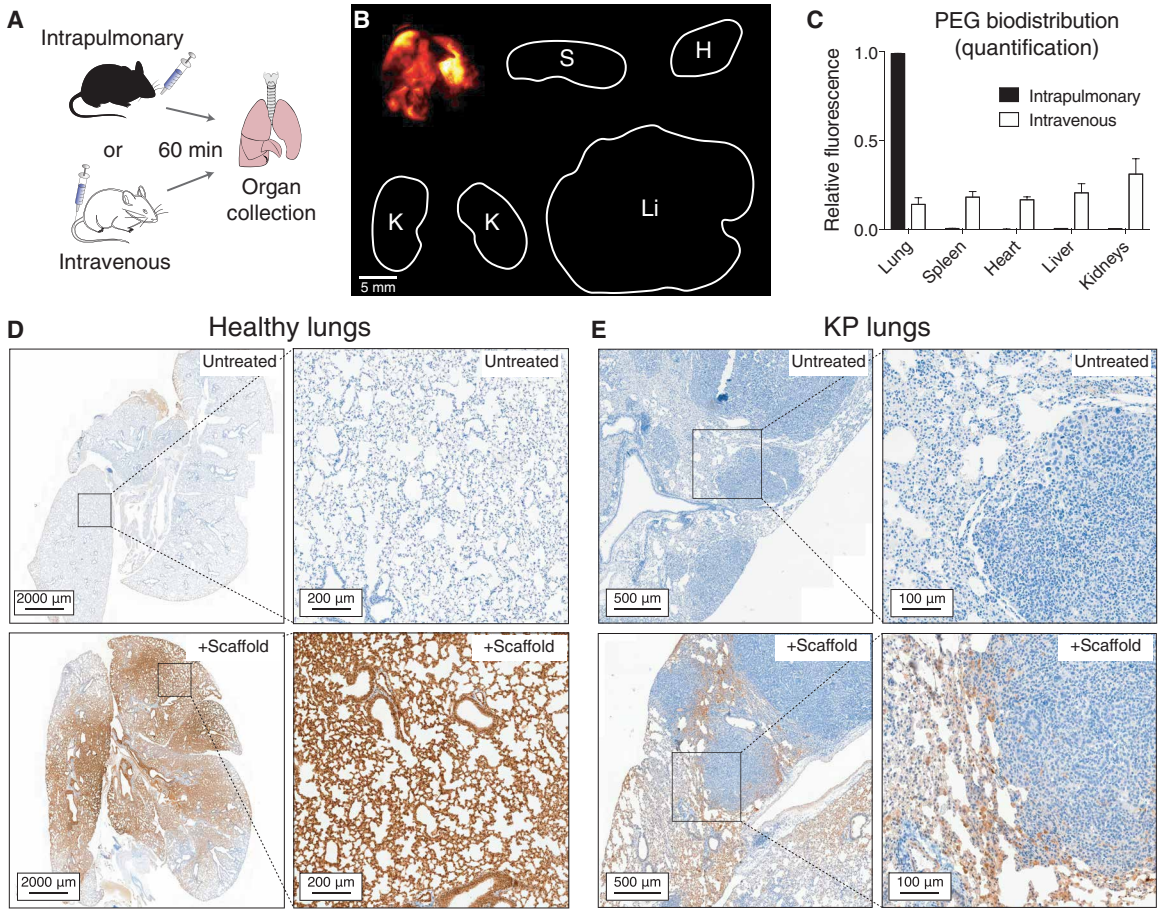

Fig. 4. Intrapulmonary-administered nanoparticle scaffolds penetrate deep within the lung and reach the periphery of KP tumors. (**A**) Wild-type mice were treated intratracheally or intravenously with VT750-labeled PEG-8_{40kDa}, and biodistribution was assessed. (**B**) Fluorescence imaging of organs was performed 60 min after intratracheal delivery. Clockwise from top-left: lung, spleen, heart, liver, and kidneys. (**C**) Organ-specific biodistribution was quantified ($n = 4$ each condition). Error bars represent SDs. (**D**) Healthy mice were either untreated (above; $n = 1$) or treated with intratracheal administration of biotin-labeled PEG scaffold (below; $n = 2$), followed by excision of lungs and immunohistochemical staining for biotin (brown). (**E**) Advanced-stage (16.5 weeks) KP mice were either untreated (top; $n = 3$) or treated with intratracheal administration of biotin-labeled PEG scaffold (bottom; $n = 3$), followed by excision of lungs and immunohistochemical staining as in (D).

differentiated KP mice from healthy controls, with some reporter differences (for example, PP03 and PP11) becoming amplified over time (Fig. 5B). At 7.5 and 10.5 weeks, 5 of 14 reporters were significantly different between KP and healthy mice ($P_{adj} < 0.05$), whereas none of the reporters differed at 5 weeks (fig. S10). In contrast, intratracheal administration of the same 14-plex panel to mice bearing flank xenograft tumors (average tumor volume of 448 mm^3) derived from a human colorectal cancer cell line yielded no differential urinary reporters between xenograft and control mice (fig. S11, A and B). Of the five reporters enriched in $KP_{7.5wk}$ urine, three (PP02, PP03, and PP09) were also enriched in $KP_{10.5wk}$ urine, and these sequences corresponded to peptides cleaved by metalloproteases or both metalloproteases and aspartic proteases in vitro. However, the most significantly enriched reporter in the urine of KP mice at 10.5 weeks (PP11; $P_{adj} = 0.0001$) corresponded to a peptide cleaved only by serine proteases in vitro. Unsupervised dimensionality reduction by principal components analysis (PCA) separated most KP and control mice at 7.5 and 10.5 weeks, but not at 5 weeks (Fig. 5, C to E).

Although the KP model is a well-established, autochthonous model of LUAD, it only represents one subset of human disease. We sought to assess the generalizability of activity-based nanosensors to other genetic subtypes by leveraging the EA model (*34*), an autochthonous model in which intrapulmonary administration of adenovirus encoding two short guide RNAs and Cas9 results in translocation and fusion of the *Eml4* and *Alk* genes, yielding LUAD that histologically resembles human disease. We administered the same panel of 14 nanosensors in EA mice 5, 7.5, and 10.5 weeks after adenoviral induction and found differential urinary reporter signatures at all three time points (fig. S12A), enabling separation of diseased mice from healthy controls at all three time points, as revealed by PCA (fig. S12B). Although several reporters were differentially enriched in the urine of both KP and EA mice, others were unique to one model; the consistent enrichment of PP01, a robust metalloprotease-specific nanosensor in EA mice but not in KP mice (fig. S10), suggests differential regulation of a subset of metalloproteases in these two models.

Activity-based nanosensor cleavage signatures are distinct in malignant and benign disease models

Existing lung cancer diagnostic modalities like LDCT suffer from high false-positive rates, resulting in cost, anxiety, and morbidity to patients due to unnecessary invasive follow-up procedures (*5*). We hypothesized that multiplexed measurements of pulmonary protease

Table 1. Reporter and substrate sequences for in vivo urinary diagnostics. ANP, 3-amino-3-(2-nitro-phenyl)propionic acid; Cha, 3-cyclohexylalanine; Cys(Me), methyl-cysteine; lowercase letters, D-amino acids.

Name	Reporter	Photolabile group	Substrate	Nanocarrier
PP01	e(+2G)(+6V)ndneeGFFsAr	ANP	GGPQGIWGQC	PEG-8_{40kDa}
PP02	eG(+6V)ndneeGF(+1F)s(+1A)r	ANP	GGPVGLIGC	PEG-8_{40kDa}
PP03	e(+3G)(+1V)ndneeGFFs(+4A)r	ANP	GGPVPLSLVMC	PEG-8_{40kDa}
PP04	e(+2G)Vndnee(+2G)FFs(+4A)r	ANP	GGPLGLRSWC	PEG-8_{40kDa}
PP05	eGVndnee(+3G)(+1F)Fs(+4A)r	ANP	GGPLGVRGKC	PEG-8_{40kDa}
PP06	e(+2G)(+6V)ndnee(+3G)(+1F)(+1F)s(+1A)r	ANP	GGfPRSGGGC	PEG-8_{40kDa}
PP07	eG(+6V)ndnee(+3G)(+1F)Fs(+4A)r	ANP	GGLGPKGQTGC	PEG-8_{40kDa}
PP08	e(+3G)(+1V)ndneeG(+10F)FsAr	ANP	GGGSGRSANAKGC	PEG-8_{40kDa}
PP09	eGVndneeGF(+10F)s(+4A)r	ANP	GGKPISLISSGC	PEG-8_{40kDa}
PP10	e(+2G)(+6V)ndneeG(+10F)(+1F)s(+1A)r	ANP	GGILSRIVGGGC	PEG-8_{40kDa}
PP11	e(+3G)(+1V)ndnee(+2G)(+10F)Fs(+4A)r	ANP	GGSGSKIIGGGC	PEG-8_{40kDa}
PP12	eGVndneeG(+10F)(+10F)sAr	ANP	GGPLGMRGGC	PEG-8_{40kDa}
PP13	e(+2G)(+6V)ndnee(+3G)(+10F)(+1F)s(+4A)r	ANP	GGP-(Cha)-G-Cys(Me)-HAGC	PEG-8_{40kDa}
PP14	e(+3G)(+1V)ndnee(+2G)(+10F)(+10F)sAr	ANP	GGAPFEMSAGC	PEG-8_{40kDa}

activity would enable discrimination of malignant from benign disease. To assess the specificity of activity-based nanosensors for lung cancer versus benign inflammatory disease, we leveraged a well-established model of lung inflammation, induced by intratracheal administration of lipopolysaccharide (LPS) (*35*). We found that several reporters were differentially enriched in the urine of $KP_{7.5wk}$ mice (fig. S13A) and $EA_{7.5wk}$ mice (fig. S13B) relative to LPS-treated mice, enabling separation of KP, EA, LPS, and healthy mice by PCA (fig. S13C).

Machine learning classification enables sensitive and specific lung cancer detection

Having demonstrated that activity-based nanosensors enable detection of two autochthonous models of LUAD, with cleavage patterns that were distinct from LPS-induced lung inflammation, we leveraged machine learning to build a classifier that could be prospectively applied to enable disease diagnosis. We trained a random forest classifier (*36*) using the urinary reporter output from a subset of $KP_{7.5wk}$ ($n = 6$), $EA_{7.5wk}$ ($n = 6$), and healthy ($n = 12$) mice and tested its ability to classify each LUAD model from healthy control mice in an independent test cohort consisting of mice that were not included in classifier training ($n = 5$ to 31; see table S3 for cohort compositions). Area under the ROC curve analysis revealed robust classification of $KP_{7.5wk}$ and $KP_{10.5wk}$ ($AUC_{7.5wks} = 0.95$ and $AUC_{10.5wks} = 0.93$) (Fig. 6A), as well as EA mice at all three time points ($AUC_{5wks} = 0.96$, $AUC_{7.5wks} = 0.98$, and $AUC_{10.5wks} = 0.93$) (Fig. 6B). We also evaluated the classifier on a test cohort that combined both LUAD models (table S3) and again found robust classification at 7.5 and 10.5 weeks ($AUC_{7.5wks} = 0.97$ and $AUC_{10.5wks} = 0.93$) (Fig. 6C). Last, we sought to determine whether a classifier could be built to distinguish lung cancer-bearing mice from both healthy mice and mice with benign lung inflammation. We trained a second classifier incorporating $KP_{7.5wk}$, $EA_{7.5wk}$, LPS-treated, and healthy control mice (table S3), applied it to an independent test cohort, and found that it performed with high accuracy in discriminating $KP_{7.5wk}$, $EA_{7.5wk}$, and a combination of the two (termed "$LUAD_{7.5wk}$") from healthy and LPS-treated mice ($AUC_{KP} = 0.97$, $AUC_{EA} = 0.98$, and $AUC_{LUAD} = 0.97$) (Fig. 6D). Together, these data illustrate the power of multiplexed, lung-specific activity-based nanosensors for sensitive and specific detection of localized lung cancer.

DISCUSSION

In this work, we present an advance toward clinical translation of a new class of biomarkers, activity-based nanosensors. We found that such multiplexed nanosensors, when delivered by intratracheal instillation, performed with specificity of 100% and sensitivity up to 95% for detection of localized disease in two autochthonous LUAD models representing *Kras/Trp53* and *Alk*-mutant disease. Furthermore, we found that LPS-induced lung inflammation did not result in false positives. Our approach overcomes the intrinsic sensitivity limitation of blood-based diagnostic assays for localized disease by profiling disease activity directly within the tumor microenvironment and providing multiple steps of signal amplification (*22*). Using intrapulmonary delivery, we further ensured that virtually all nanosensors reached the lung and bypassed nonspecific activation in off-target organs.

This study represents a step toward clinical implementation of activity-based nanosensors for lung cancer testing, validating the efficacy of the tool in two autochthonous, immunocompetent models of localized LUAD. The use of genetically engineered mouse models offered several advantages over cell transplant models, including the ability to explore stage-specific differences, as well as proteolytic contributions from immune cells. Activity-based nanosensors detected disease as early as 7.5 weeks after initiating the KP model, when only grade 1 AAH and grade 2 adenomas are present (*24*). Furthermore, although metalloprotease-sensitive nanosensors were, as expected, preferentially cleaved in KP mice at both 7.5 and 10.5 weeks, the activation of PP11 (a serine protease-sensitive substrate) in $KP_{10.5wk}$ mice could point to an unexpected role of serine protease activity in tumor progression at this disease stage. One hypothesis is that tumor-infiltrating immune cells, which secrete a multitude of serine proteases (*37*), may contribute to nanosensor cleavage in $KP_{10.5wk}$ mice. Neutrophils

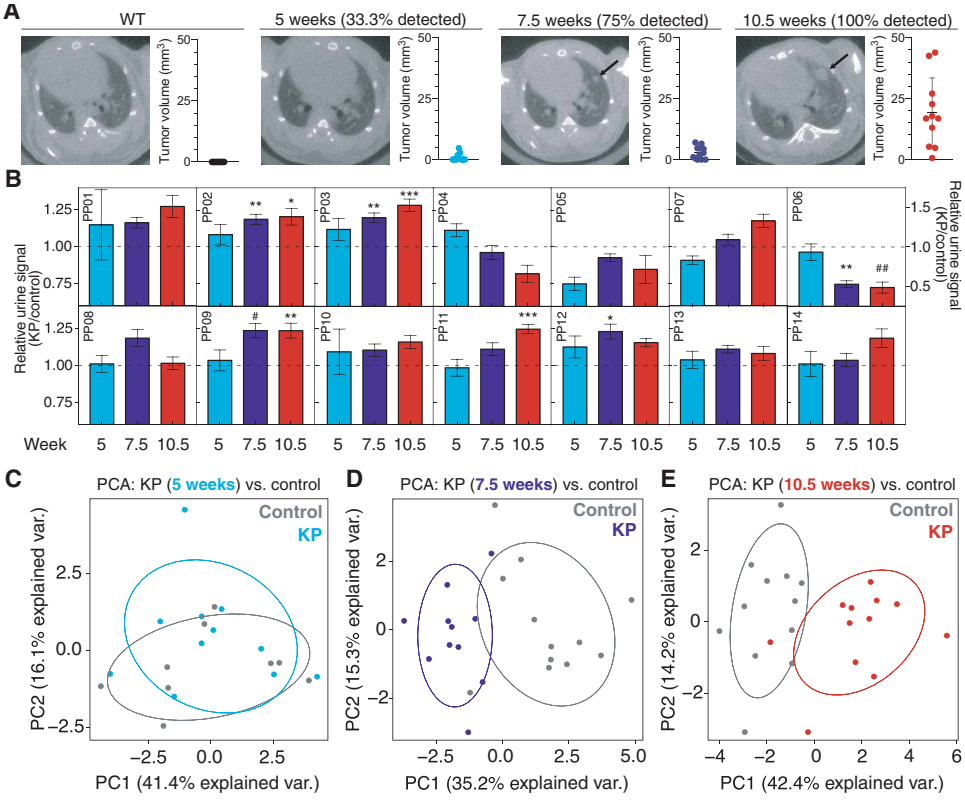

Fig. 5. Activity-based nanosensors distinguish between diseased and healthy mice. (**A**) Tumor development was monitored by microCT in healthy (left; $n = 11$) and KP_{5wk} ($n = 12$), $KP_{7.5wk}$ ($n = 12$), and $KP_{10.5wk}$ ($n = 11$) mice. The right three panels represent time series of a single mouse, with arrow indicating development of a single nodule over time. The quantification of tumor volume is shown to the right of each image, and the percentage of mice with detectable tumors at each time point (% detected) is shown above each panel. (**B**) Urine output of activity-based nanosensors administered to KP and control animals at 5 weeks (KP, $n = 11$; control, $n = 9$), 7.5 weeks (KP, $n = 11$; control, $n = 12$), and 10.5 weeks (KP, $n = 12$; control, $n = 12$) after tumor induction. For clarity, PP06 is presented on a larger-scale *y* axis. $^{*}P_{adj} < 0.05$, $^{**}P_{adj} < 0.01$, and $^{***}P_{adj} < 0.001$ by two-tailed *t* test with Holm-Sidak correction; $\#P_{adj} < 0.05$ and $\#\#P_{adj} < 0.01$ by Mann-Whitney test with Bonferroni correction. Error bars represent SEMs. (**C** to **E**) PCA of mean-normalized urinary reporters for KP mice and controls at 5 weeks (KP, $n = 11$; control, $n = 9$) (C), 7.5 weeks (KP, $n = 11$; control, $n = 12$) (D), and 10.5 weeks (KP, $n = 12$; control, $n = 12$) (E).

are known to infiltrate KP tumors around 10 weeks after tumor induction (*38*). The potential capacity of activity-based nanosensors to measure immune-mediated protease activity (*18*) raises the prospect of rapid, noninvasive, and longitudinal immunotherapy response monitoring.

Here, we report improved sensitivity of activity-based nanosensors relative to previous work by our group, as well as existing and emerging blood-based diagnostics for cancer. We found that our nanosensors could detect tumors in $KP_{7.5wk}$ mice, whose total tumor volumes were, on average, only 2.78 mm^3, more than an order of magnitude smaller than our most sensitive method to date (36 mm^3 in an ovarian cancer model) (*16*). By comparison, in the LS174T colorectal cancer xenograft model, ctDNA is detectable when tumor volumes reach 1000 mm^3 (*39*), carcinoembryonic antigen is detectable around 135 to 330 mm^3 (*12*, *39*), and intravenously administered activity-based nanosensors have previously been shown to detect disease in this model around 130 mm^3 (*12*). Last, in the autochthonous $Kras^{G12D}$-mutant "K" lung cancer model, ctDNA bearing the $Kras^{G12D}$ mutation was only detectable when average tumor volumes were 7.1 mm^3 (*40*), even with collection of 2.5% of the total mouse blood volume, scaling to 125 ml in humans.

In the NLST, 96.4% of positive LDCT findings were false positives (*3*, *5*), and many of these patients went on to suffer major complications during invasive follow-up procedures (*4*, *5*). Therefore, there is a need to develop noninvasive diagnostic methods that can distinguish between lung cancer and benign lung disease. Here, we demonstrated the specificity of activity-based nanosensors for lung cancer, rather than benign lung inflammation, through multiplexing and machine learning. Although fewer than half of the 14 reporters were differentially enriched in the urine of KP mice and healthy controls, several more had diagnostic power in EA mice, and others were informative in the classification of malignant versus inflammatory disease. As a result, we found that a pretrained random forest classifier could distinguish between lung cancer-bearing mice (regardless of subtype) and benign disease controls. Although a clinical study would be necessary to directly assess the effectiveness of activity-based nanosensors in the setting of LDCT lung cancer screening, our results suggest that activity-based nanosensors may complement LDCT for discrimination of malignant lesions from benign disease.

Although this work represents a step toward translation of activity-based nanosensors for lung cancer detection, there are limitations that must be addressed before clinical implementation. In this work, we demonstrated the sensitivity and specificity of intrapulmonary activity-based nanosensors for localized lung cancer in two genetically engineered mouse models of LUAD. Although the advantages of such models over xenograft models in recapitulating human disease are numerous (*41*), mouse models cannot fully capture the native oncogenic properties or heterogeneity found in human lung cancer, and further in vivo validation is needed to confirm the generalizability of activity-based nanosensors to other lung cancer subtypes. Similarly, although activity-based nanosensors can discriminate between lung cancer and LPS-driven lung inflammation, it is possible that clinical lung cancer testing may be confounded by other benign lung disease etiologies or chronic exposure to tobacco smoke. Because of the inherent limitations of mouse models, clinical trials will be necessary to fully validate the robustness of activity-based nanosensors in detecting lung cancer and distinguishing malignant from benign and extrapulmonary disease in humans. Last, the intrapulmonary delivery methods presented here must be optimized before clinical translation. Here, we delivered activity-based nanosensors by intratracheal instillation and demonstrated their stability after aerosolization. However, a clinically relevant intrapulmonary delivery method such as dry

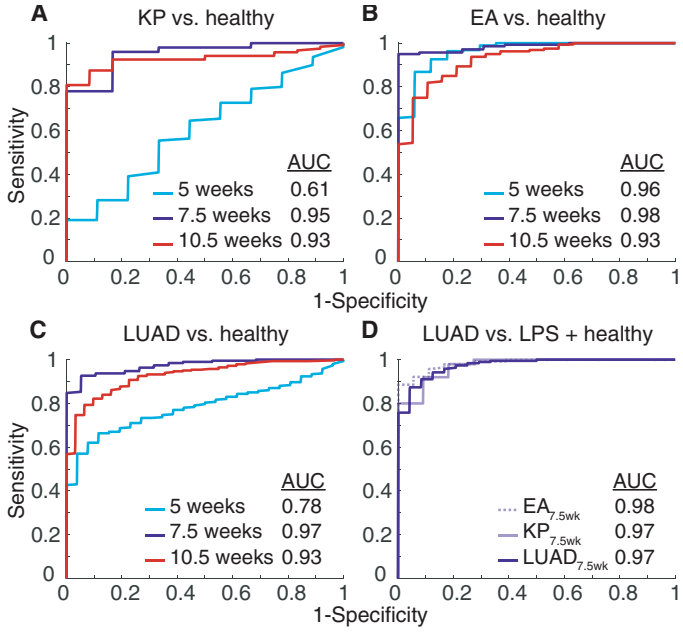

Fig. 6. Machine learning enables sensitive and specific classification of two genetic subtypes of LUAD. (**A** to **C**) ROC curves showing performance of a single random forest classifier trained on urinary reporters from a subset of $KP_{7.5wk}$, $EA_{7.5wk}$, and healthy controls in discriminating an independent test cohort of KP (A), EA (B), or a combination of KP and EA (C) mice from healthy controls at all three time points. (**D**) ROC curve showing performance of a random forest classifier trained on urinary reporters from $KP_{7.5wk}$ and $EA_{7.5wk}$ mice versus LPS and healthy control mice in discriminating an independent test cohort of $KP_{7.5wk}$, $EA_{7.5wk}$, and a combination of the two (termed "LUAD") from healthy and LPS-treated mice. All ROC curves are averages over 10 independent train-test trials and show the results in the test cohort. $n = 5$ to 31; details of cohort sample sizes are shown in table S3.

powder inhalation or nebulization will be required for clinical implementation.

In summary, intrapulmonary activity-based nanosensors perform with high sensitivity and specificity for detection of localized lung cancer in autochthonous mouse models via a noninvasive urine test. To engineer these nanosensors, we leveraged analysis of LUAD gene expression datasets to nominate candidate proteases, screened these proteases in vitro against a panel of peptide substrates, and directly delivered nanosensors carrying these substrates into the lungs of mice. Activity-based nanosensors may have clinical utility as a rapid, safe, and cost-effective follow-up to LDCT, reducing the number of patients referred for invasive testing. With further optimization and validation studies, activity-based nanosensors may one day provide an accurate, noninvasive, and radiation-free strategy for lung cancer testing.

MATERIALS AND METHODS

Study design

The goal of this study was to determine whether intrapulmonary administration of a multiplexed library of activity-based nanosensors could be used to sensitively and specifically detect lung cancer in autochthonous mouse models. All animal studies were approved by the Massachusetts Institute of Technology (MIT) committee on animal care (protocol 0417-025-20) and were conducted in compliance with institutional and national policies. Reporting was in compliance with Animal Research: Reporting In Vivo Experiments (ARRIVE) guidelines. Experiments involving intrapulmonary delivery of activity-based nanosensors in KP mice consisted of 12 KP mice and 12 healthy control mice; experiments involving intrapulmonary delivery of activity-based nanosensors in EA mice consisted of 20 EA mice and 20 healthy control mice. These mice were monitored, by intratracheal nanosensor administration and microCT, at 5, 7.5, and 10.5 weeks after tumor induction. Sample size was selected to ensure a sample size greater than or equal to five for both training and test groups at each time point and for each treatment group. Urine samples with peak area ratio (PAR) values of zero for two or more analytes were excluded because these samples represented failed nanosensor deliveries and would confound analysis. For differential expression analysis of protease genes in KP mice, genes for which neither normal lung sample was nonzero were excluded, as calculation of fold changes (tumor/normal) would otherwise yield undefined values. For ROC analysis in the LGRC dataset, genes for which greater than half of the samples had fragments per kilobase of transcript per million mapped reads (FPKM) values of zero were excluded. During selection of KP and healthy control mice, investigators were blinded to all characteristics but age, sex, and genotype. For random forest classification, mice were randomly assigned to training and test cohorts using a randomly generated seed.

Statistical analysis

For RNA-seq data, binary classification using a GLM was performed using the Caret package (*42*) in the R statistical environment (*43*). Prespecified training and testing cohorts were randomly assigned, with 75 and 25% of samples used for training and testing, respectively. For all urine experiments, PAR values were normalized to nanosensor stock concentrations and then mean normalized across all reporters in a given urine sample before further statistical analysis. To identify differential urinary reporters, all reporters were first tested for normality by Kolmogorov-Smirnov normality test with Dallal-Wilkinson-Lilliefors *P* value. All normally distributed reporters were analyzed by unpaired two-tailed *t* test, followed by correction for multiple hypotheses using the Holm-Sidak method, and non-normal reporters were analyzed by Mann-Whitney test with Bonferroni correction in GraphPad Prism 7.0. $P_{adj} < 0.05$ was considered significant. PCA was performed on mean-normalized PAR values and implemented in MATLAB R2019b (MathWorks). For disease classification based on urinary activity-based nanosensor signatures, randomly assigned sets of paired data samples consisting of features (the mean-normalized PAR values) and labels (for example, KP and EA) were used to train random forest (*36*) classifiers implemented with the TreeBagger class in MATLAB R2019b. Estimates of out-of-bag error were used for cross-validation, and trained classifiers were tested on randomly assigned, held-out, independent test cohorts. The specific composition of train-test cohorts is provided in table S3. Ten independent train-test trials were run for each classification problem, and classification performance was evaluated with ROC statistics calculated in MATLAB. Classifier performance was reported as the mean accuracy and AUC across the 10 independent trials.

SUPPLEMENTARY MATERIALS

stm.sciencemag.org/cgi/content/full/12/537/eaaw0262/DC1

Methods

Fig. S1. KP model genetically and histologically recapitulates human lung adenocarcinoma.

Fig. S2. Human LUAD-associated proteases are not overexpressed in benign lung diseases.

Fig. S3. LUAD protease panel genes are enriched across genetic and histological lung cancer subtypes.

Fig. S4. Peptide substrates are cleaved by one or a combination of metallo, serine, and aspartic proteases.
Fig. S5. Clearance of PEG-8_{40kDa} nanoparticles from lungs follows single phase exponential decay kinetics.
Fig. S6. No toxicity is observed in mice treated with intrapulmonary activity-based nanosensors.
Fig. S7. Activity-based nanosensors are stable to aerosolization.
Fig. S8. Aerosolized nanoparticles penetrate deep within the lung and avoid distribution to off-target organs.
Fig. S9. Free reporters enter the bloodstream after pulmonary delivery and are detectable in the urine by mass spectrometry.
Fig. S10. Multiple reporters are differentially enriched in the urine of healthy mice and KP mice at 7.5 and 10.5 weeks.
Fig. S11. Extrapulmonary disease is undetectable by intrapulmonary activity-based nanosensors.
Fig. S12. Intrapulmonary activity-based nanosensors differentiate mice bearing Alk-driven lung cancer from healthy controls.
Fig. S13. Pulmonary activity-based nanosensor cleavage profile is distinct in lung cancer and benign lung inflammation.
Table S1. Reporter and substrate sequences for in vitro recombinant protease screen.
Table S2. Quantification of tumor burden in KP mice by microCT.
Table S3. Composition of training and test cohorts for random forest classification.
Data file S1. Raw data from figures.

View/request a protocol for this paper from *Bio-protocol*.

REFERENCES AND NOTES

1. N. Howlader, A. Noone, M. Krapcho, D. Miller, A. Brest, M. Yu, J. Ruhl, Z. Tatalovich, A. Mariotto, D. Lewis, H. Chen, E. Feuer, K. Cronin, *SEER Cancer Statistics Review, 1975–2016* (National Cancer Institute, 2018).
2. L. T. Tanoue, N. T. Tanner, M. K. Gould, G. A. Silvestri, Lung cancer screening. *Am. J. Respir. Crit. Care Med.* **191**, 19–33 (2015).
3. National Lung Screening Trial Research Team, D. R. Aberle, A. M. Adams, C. D. Berg, W. C. Black, J. D. Clapp, R. M. Fagerstrom, I. F. Gareen, C. Gatsonis, P. M. Marcus, J. D. Sicks, Reduced lung-cancer mortality with low-dose computed tomographic screening. *N. Engl. J. Med.* **365**, 395–409 (2011).
4. W. C. Black, I. F. Gareen, S. S. Soneji, J. D. Sicks, E. B. Keeler, D. R. Aberle, A. Naeim, T. R. Church, G. A. Silvestri, J. Gorelick, C. Gatsonis; National Lung Screening Trial Research Team, Cost-Effectiveness of CT screening in the National Lung Screening Trial. *N. Engl. J. Med.* **371**, 1793–1802 (2014).
5. P. B. Bach, J. N. Mirkin, T. K. Oliver, C. G. Azzoli, D. A. Berry, O. W. Brawley, T. Byers, G. A. Colditz, M. K. Gould, J. R. Jett, A. L. Sabichi, R. Smith-Bindman, D. E. Wood, A. Qaseem, F. C. Detterbeck, Benefits and harms of CT screening for lung cancer: A systematic review. *JAMA* **307**, 2418–2429 (2012).
6. R. S. Wiener, D. C. Wiener, M. K. Gould, Risks of transthoracic needle biopsy: How high? *Clin. Pulm. Med.* **20**, 29–35 (2013).
7. M. Oudkerk, A. Devaraj, R. Vliegenthart, T. Henzler, H. Prosch, C. P. Heussel, G. Bastarrika, N. Sverzellati, M. Mascalchi, S. Delorme, D. R. Baldwin, M. E. Callister, N. Becker, M. A. Heuvelmans, W. Rzyman, M. V. Infante, U. Pastorino, J. H. Pedersen, E. Paci, S. W. Duffy, H. de Koning, J. K. Field, European position statement on lung cancer screening. *Lancet Oncol.* **18**, e754–e766 (2017).
8. A. M. Newman, S. V. Bratman, J. To, J. F. Wynne, N. C. Eclov, L. A. Modlin, C. L. Liu, J. W. Neal, H. A. Wakelee, R. E. Merritt, J. B. Shrager, B. W. Loo, A. A. Alizadeh, M. Diehn, An ultrasensitive method for quantitating circulating tumor DNA with broad patient coverage. *Nat. Med.* **20**, 548–554 (2014).
9. J. C. M. Wan, C. Massie, J. Garcia-Corbacho, F. Mouliere, J. D. Brenton, C. Caldas, S. Pacey, R. Baird, N. Rosenfeld, Liquid biopsies come of age: Towards implementation of circulating tumour DNA. *Nat. Rev. Cancer* **17**, 223–238 (2017).
10. I. S. Haque, O. Elemento, Challenges in using ctDNA to achieve early detection of cancer. bioRxiv 237578 [**Preprint**]. 2017.
11. G. A. Silvestri, A. Vachani, D. Whitney, M. Elashoff, K. Porta Smith, J. S. Ferguson, E. Parsons, N. Mitra, J. Brody, M. E. Lenburg, A. Spira; AEGIS Study Team, A bronchial genomic classifier for the diagnostic evaluation of lung cancer. *N. Engl. J. Med.* **373**, 243–251 (2015).
12. G. A. Kwong, G. von Maltzahn, G. Murugappan, O. Abudayyeh, S. Mo, I. A. Papayannopoulos, D. Y. Sverdlov, S. B. Liu, A. D. Warren, Y. Popov, D. Schuppan, S. N. Bhatia, Mass-encoded synthetic biomarkers for multiplexed urinary monitoring of disease. *Nat. Biotechnol.* **31**, 63–70 (2013).
13. K. Y. Lin, G. A. Kwong, A. D. Warren, D. K. Wood, S. N. Bhatia, Nanoparticles that sense thrombin activity as synthetic urinary biomarkers of thrombosis. *ACS Nano* **7**, 9001–9009 (2013).
14. A. D. Warren, S. T. Gaylord, K. C. Ngan, M. D. Milutinovic, G. A. Kwong, S. N. Bhatia, D. R. Walt, Disease detection by ultrasensitive quantification of microdosed synthetic urinary biomarkers. *J. Am. Chem. Soc.* **136**, 13709–13714 (2014).
15. A. D. Warren, G. A. Kwong, D. K. Wood, K. Y. Lin, S. N. Bhatia, Point-of-care diagnostics for noncommunicable diseases using synthetic urinary biomarkers and paper microfluidics. *Proc. Natl. Acad. Sci. U.S.A.* **111**, 3671–3676 (2014).
16. E. J. Kwon, J. S. Dudani, S. N. Bhatia, Ultrasensitive tumour-penetrating nanosensors of protease activity. *Nat. Biomed. Eng.* **1**, 0054 (2017).
17. J. S. Dudani, M. Ibrahim, J. Kirkpatrick, A. D. Warren, S. N. Bhatia, Classification of prostate cancer using a protease activity nanosensor library. *Proc. Natl. Acad. Sci. U.S.A.* **115**, 8954–5989 (2018).
18. C. G. Buss, J. S. Dudani, R. T. K. Akana, H. E. Fleming, S. N. Bhatia, Protease activity sensors noninvasively classify bacterial infections and antibiotic responses. *EBioMedicine* **38**, 248–256 (2018).
19. C. N. Loynachan, A. P. Soleimany, J. S. Dudani, Y. Lin, A. Najer, A. Bekdemir, Q. Chen, S. N. Bhatia, M. M. Stevens, Renal clearable catalytic gold nanoclusters for in vivo disease monitoring. *Nat. Nanotechnol.* **14**, 883–890 (2019).
20. D. Hanahan, R. A. Weinberg, Hallmarks of cancer: The next generation. *Cell* **144**, 646–674 (2011).
21. J. S. Dudani, A. D. Warren, S. N. Bhatia, Harnessing protease activity to improve cancer care. *Annu. Rev. Cancer Biol.* **2**, 353–376 (2018).
22. G. A. Kwong, J. S. Dudani, E. Carrodeguas, E. V. Mazumdar, S. M. Zekavat, S. N. Bhatia, Mathematical framework for activity-based cancer biomarkers. *Proc. Natl. Acad. Sci.* **112**, 12627–12632 (2015).
23. R. S. Herbst, J. V. Heymach, S. M. Lippman, Lung cancer. *N. Engl. J. Med.* **359**, 1367–1380 (2008).
24. M. DuPage, A. L. Dooley, T. Jacks, Conditional mouse lung cancer models using adenoviral or lentiviral delivery of Cre recombinase. *Nat. Protoc.* **4**, 1064–1072 (2009).
25. C. H. Chuang, P. G. Greenside, Z. N. Rogers, J. J. Brady, D. Yang, R. K. Ma, D. R. Caswell, S. Chiou, A. F. Winters, B. M. Grüner, G. Ramaswami, A. L. Spencley, K. E. Kopecky, L. C. Sayles, E. A. Sweet-cordero, J. B. Li, A. Kundaje, M. M. Winslow, Molecular definition of a metastatic lung cancer state reveals a targetable CD109–Janus kinase–Stat axis. *Nat. Med.* **23**, 291–300 (2017).
26. A. Sweet-Cordero, S. Mukherjee, A. Subramanian, H. You, J. J. Roix, C. Ladd-Acosta, J. Mesirov, T. R. Golub, T. Jacks, An oncogenic KRAS2 expression signature identified by cross-species gene-expression analysis. *Nat. Genet.* **37**, 48–55 (2005).
27. V. G. Tusher, R. Tibshirani, G. Chu, Significance analysis of microarrays applied to the ionizing radiation response. *Proc. Natl. Acad. Sci. U.S.A.* **98**, 5116–5121 (2001).
28. The Cancer Genome Atlas Research Network, Comprehensive molecular profiling of lung adenocarcinoma. *Nature* **511**, 543–550 (2014).
29. M. I. Love, W. Huber, S. Anders, Moderated estimation of fold change and dispersion for RNA-seq data with DESeq2. *Genome Biol.* **15**, 550 (2014).
30. V. K. Mootha, C. M. Lindgren, K.-F. Eriksson, A. Subramanian, S. Sihag, J. Lehar, P. Puigserver, E. Carlsson, M. Ridderstråle, E. Laurila, N. Houstis, M. J. Daly, N. Patterson, J. P. Mesirov, T. R. Golub, P. Tamayo, B. Spiegelman, E. S. Lander, J. N. Hirschhorn, D. Altshuler, L. C. Groop, PGC-1α-responsive genes involved in oxidative phosphorylation are coordinately downregulated in human diabetes. *Nat. Genet.* **34**, 267–273 (2003).
31. R. L. Kusko, J. F. Brothers, J. Tedrow, K. Pandit, L. Huleihel, C. Perdomo, G. Liu, B. Juan-Guardela, D. Kass, S. Zhang, M. Lenburg, F. Martinez, J. Quackenbush, F. Sciurba, A. Limper, M. Geraci, I. Yang, D. A. Schwartz, J. Beane, A. Spira, N. Kaminski, Integrated genomics reveals convergent transcriptomic networks underlying chronic obstructive pulmonary disease and idiopathic pulmonary fibrosis. *Am. J. Respir. Crit. Care Med.* **194**, 948–960 (2016).
32. T. Ueno, S. Linder, G. Elmberger, Aspartic proteinase napsin is a useful marker for diagnosis of primary lung adenocarcinoma. *Br. J. Cancer* **88**, 1229–1233 (2003).
33. P. Thomas, R. Khokha, F. A. Shepherd, R. Feld, M. S. Tsao, Differential expression of matrix metalloproteinases and their inhibitors in non-small cell lung cancer. *J. Pathol.* **190**, 150–156 (2000).
34. D. Maddalo, E. Manchado, C. P. Concepcion, C. Bonetti, J. A. Vidigal, Y. C. Han, P. Ogrodowski, A. Crippa, N. Rekhtman, E. De Stanchina, S. W. Lowe, A. Ventura, In vivo engineering of oncogenic chromosomal rearrangements with the CRISPR/Cas9 system. *Nature* **516**, 423–428 (2014).
35. V. Poroyko, F. Meng, A. Meliton, T. Afonyushkin, A. Ulanov, E. Semenyuk, O. Latif, V. Tesic, A. A. Birukova, K. G. Birukov, Alterations of lung microbiota in a mouse model of LPS-induced lung injury. *Am. J. Physiol. Cell. Mol. Physiol.* **309**, L76–L83 (2015).
36. L. Breiman, Random forests. *Mach. Learn.* **45**, 5–32 (2001).
37. C. T. N. Pham, Neutrophil serine proteases: Specific regulators of inflammation. *Nat. Rev. Immunol.* **6**, 541–550 (2006).
38. S. E. Busch, M. L. Hanke, J. Kargl, H. E. Metz, D. MacPherson, A. M. Houghton, Lung cancer subtypes generate unique immune responses. *J. Immunol.* **197**, 4493–4503 (2016).

39. A. Aalipour, H.-Y. Chuang, S. Murty, A. L. D'Souza, S.-m. Park, G. S. Gulati, C. B. Patel, C. Beinat, F. Simonetta, I. Martinić, G. Gowrishankar, E. R. Robinson, E. Aalipour, Z. Zhian, S. S. Gambhir, Engineered immune cells as highly sensitive cancer diagnostics. *Nat. Biotechnol.* **37**, 531–539 (2019).
40. C. P. Rakhit, R. M. Trigg, J. Le Quesne, M. Kelly, J. A. Shaw, C. Pritchard, L. M. Martins, Early detection of pre-malignant lesions in a KRAS G12D-driven mouse lung cancer model by monitoring circulating free DNA. *Dis. Model. Mech.* **12**, dmm036863 (2019).
41. K. Kersten, K. E. Visser, M. H. Miltenburg, J. Jonkers, Genetically engineered mouse models in oncology research and cancer medicine. *EMBO Mol. Med.* **9**, 137–153 (2017).
42. M. Kuhn, Caret: Classification and Regression Training (2017); https://cran.r-project.org/package=caret.
43. R Core Team, R: A Language and Environment for Statistical Computing (2017); https://www.r-project.org.
44. M. Reich, T. Liefeld, J. Gould, J. Lerner, P. Tamayo, J. P. Mesirov, GenePattern 2.0. *Nat. Genet.* **38**, 500–501 (2006).
45. J. Schindelin, I. Arganda-Carreras, E. Frise, V. Kaynig, M. Longair, T. Pietzsch, S. Preibisch, C. Rueden, S. Saalfeld, B. Schmid, J. Y. Tinevez, D. J. White, V. Hartenstein, K. Eliceiri, P. Tomancak, A. Cardona, Fiji: an open-source platform for biological-image analysis. *Nat Methods* **9**, 676–682 (2012).

Acknowledgments: We thank J. S. Dudani for assistance with experimental design, R. Zhao and M. Anahtar for technical assistance, A. Mancino (Syneos Health) for performing mass spectrometry, and the Koch Institute Swanson Biotechnology Center, specifically the Bioinformatics & Computing core, the Histology core, and the Preclinical Modeling, Imaging, and Testing core. **Funding:** This work was supported by a Koch Institute Support Grant P30-CA14051 from the National Cancer Institute (to T.J.), a Core Center Grant P30-ES002109 from the National Institute of Environmental Health Sciences (to S.N.B.), the Ludwig Center for Molecular Oncology at MIT (to S.N.B. and T.J.), the Koch Institute's Marble Center for Cancer Nanomedicine (to S.N.B.), the Koch Institute Frontier Research Program through a gift from Upstage Lung Cancer (to S.N.B.), and Johnson & Johnson (to S.N.B.). We acknowledge support from Ludwig Center fellowships (to J.D.K. and A.D.W.), the NSF Graduate Research Fellowships Program (to A.D.W. and A.P.S.), the NIH Molecular Biophysics Training Grant NIH/NIGMS T32 GM008313 (to A.P.S.), National Cancer Institute K99 Grant R00-CA187317 (to T.T.), and the Damon Runyon Postdoctoral Fellowship (to P.M.K.W.). S.N.B. and T.J. are HHMI investigators.
Author contributions: J.D.K., A.D.W., and S.N.B. initiated and designed the study. J.D.K., A.D.W., and A.P.S. performed experiments. A.P.S. and J.D.K. performed statistical analysis. P.M.K.W. generated animal models. J.C.V. performed microCT analysis. J.D.K. and C.M.-A. performed transcriptomic analysis. S.N.B., T.J., H.E.F., and T.T. supervised the research. J.D.K., A.D.W., and S.N.B. wrote the first draft of the manuscript. H.E.F. assisted in the preparation of the manuscript. All authors contributed to writing and editing subsequent drafts of the manuscript and approved the final manuscript. **Competing interests:** J.D.K., A.D.W., and S.N.B. are listed as inventors on a patent application (Lung protease nanosensors and uses thereof, U.S. Patent Application Number 16/582,053) related to this work. S.N.B. is a director at Vertex; is a cofounder and consultant at Glympse Bio, Satellite Bio, and Impilo Therapeutics; is a consultant for Cristal, Maverick, and Moderna; and receives sponsored research funds from Johnson & Johnson. T.J. is a member of the Board of Directors of Amgen and Thermo Fisher Scientific; is a cofounder of Dragonfly Therapeutics and T2 Biosystems; and serves on the Scientific Advisory Board of Dragonfly Therapeutics, SQZ Biotech, and Skyhawk Therapeutics. A.D.W. is an employee of Third Rock Ventures, owns equity in Thrive Earlier Detection, and holds stock options in Glympse Bio. A.D.W. also provides consulting services for Thrive Earlier Detection and was previously employed by Glympse Bio. T.J.'s laboratory currently also receives funding from Calico and Johnson & Johnson, but these funds did not support the research described in this manuscript. **Data and materials availability:** All data associated with this study are present in the paper or Supplementary Materials.

Submitted 17 December 2018
Resubmitted 6 August 2019
Accepted 11 March 2020
Published 1 April 2020
10.1126/scitranslmed.aaw0262

Citation: J. D. Kirkpatrick, A. D. Warren, A. P. Soleimany, P. M. K. Westcott, J. C. Voog, C. Martin-Alonso, H. E. Fleming, T. Tammela, T. Jacks, S. N. Bhatia, Urinary detection of lung cancer in mice via noninvasive pulmonary protease profiling. *Sci. Transl. Med.* **12**, eaaw0262 (2020).

Science Translational Medicine

Urinary detection of lung cancer in mice via noninvasive pulmonary protease profiling

Jesse D. Kirkpatrick, Andrew D. Warren, Ava P. Soleimany, Peter M. K. Westcott, Justin C. Voog, Carmen Martin-Alonso, Heather E. Fleming, Tuomas Tammela, Tyler Jacks and Sangeeta N. Bhatia

Sci Transl Med **12**, eaaw0262.
DOI: 10.1126/scitranslmed.aaw0262

Noninvasive nanoparticles for lung cancer

Previously developed nanoparticle technology has been shown to detect the hallmark protease activity of many cancers, amplifying it into a urinary readout. Now, Kirkpatrick *et al.* optimize protease activity–based nanosensors for the detection of lung cancer. Intratracheal instillation of nanosensors enabled detection of localized lung adenocarcinoma in two immunocompetent, autochthonous mouse models. The sensors distinguished between lung cancer and lung inflammation, and did not detect protease activity in a colorectal cancer xenograft model. Further work will need to confirm the approach for human lung cancer and other lung cancer subtypes and to formulate the nanosensors for intrapulmonary delivery in patients.